J. Fluid Mech. (2005), *vol.* 534, *pp.* 185–194.
doi:10.1017/S0022112005004635 Printed in the United Kingdom

Vortex-induced vibrations at subcritical *Re*

By SANJAY MITTAL AND SAURAV SINGH

Department of Aerospace Engineering, Indian Institute of Technology Kanpur, UP 208 016, India

(Received 3 August 2004 and in revised form 18 March 2005)

Flow past a stationary cylinder becomes unstable at $Re \sim 47$. Flow-induced vibrations of an elastically mounted cylinder, of low non-dimensional mass, is investigated at subcritical Reynolds numbers. A stabilized finite-element formulation is used to solve the incompressible flow equations and the cylinder motion in two dimensions. The cylinder is free to vibrate in both the transverse and in-line directions. It is found that, for certain natural frequencies of the spring–mass system, vortex shedding and self-excited vibrations of the cylinder are possible for *Re* as low as 20. Lock-in is observed in all cases. However, the mass of the oscillator plays a major role in determining the proximity of the vortex-shedding frequency to the natural frequency of the oscillator. A global linear stability analysis (LSA) for the combined flow and oscillator is carried out. The results from the LSA are in good agreement with the two-dimensional direct numerical simulations.

1. Introduction

The flow past a stationary circular cylinder becomes unstable at $Re \sim 47$. This instability, primarily due to the wake, results in von Kármán vortex shedding and causes the cylinder to experience unsteady lift and drag forces. A cylinder mounted on elastic supports may undergo vortex-induced vibrations (VIV) as a result of this unsteadiness. It is well known that the motion of the cylinder can alter the flow field significantly. Under certain conditions, the motion can cause the vortex-shedding frequency to match the vibration frequency. This is referred to as *lock-in* or *synchronization*. In addition, near the low and high ends of the lock-in regime, the flow and cylinder response may exhibit hysteresis. For a comprehensive review of the research on various aspects of VIV the reader is referred to Williamson & Govardhan (2004).

Almost all the investigations of flow-induced vibrations in the past have been conducted for $Re > Re_{c0}$, where Re_{c0} is the critical Reynolds number for the stationary cylinder. The objective of the present work is to investigate VIV for $Re < Re_{c0}$. One question of interest is whether an elastically supported cylinder in a uniform flow undergoes self-excited oscillations for $Re < Re_{c0}$. Cossu & Morino (2000), from their global stability analysis of an aeroelastic system, found that Re_c for a cylinder with fluid-to-solid density ratio larger than 1/70 is less than half that of the stationary-structure case. They identified two significant modes for the vibrating cylinder. The 'nearly structural' mode corresponds to eigenvalues which, in the limit of very small fluid/solid density ratio, tend to the characteristic (complex) frequency of the structure in the absence of fluid. The other is the von Kármán mode that corresponds to a pair of eigenvalues whose frequencies are almost identical to the leading eigenvalues of the fluid-only system with a stationary structure. At $Re = 23.512$, the von Kármán mode is stable while the nearly structural one is unstable. Buffoni (2003) found that vortex shedding could be triggered under subcritical conditions ($25 < Re < 49$) by forced transverse vibrations of the cylinder at specific frequencies. Shedding is not observed

at low frequencies at any Re. As the frequency is increased, the intensity of the vortex shedding increases to its maximum level and then disappears. A relationship between Re and the frequency at which the shedding is intense has been proposed. In the present work, direct time integration of the flow equations along with the equations of motion for the cylinder is carried out to investigate the aeroelastic instability for $Re < Re_{c0}$. The critical parameters, at the onset of the instability, are confirmed via a global linear stability analysis. A stabilized space–time finite element formulation (Tezduyar, Behr & Liou 1992*a*; Tezduyar *et al.* 1992*b*; Mittal & Tezduyar 1992) has been utilized to solve the governing equations.

To encourage high-amplitude oscillations, the structural damping coefficient is assigned a zero value and an oscillator with very low non-dimensional mass ($M = 4.73$) is considered. The cylinder is allowed to vibrate in both transverse and in-line directions. First, computations for a system with fixed mass and natural frequency, f_n, are carried out for various Re. In this case, the reduced natural frequency, $F_n = f_n D/U_\infty$, varies inversely with Re. Here, D is the diameter of the cylinder and U_∞ the free-stream flow speed. To investigate the effect of Re and F_n independently two sets of computations are carried out. In the first the Reynolds number is fixed ($Re = 33$) and the reduced velocity, ($U^* = 1/F_n$) is varied. In the second, the reduced velocity of the system is fixed at $U^* = 7.84$ ($F_n = 0.1275$) and the effect of Reynolds number ($15 \leqslant Re \leqslant 90$) is investigated.

2. The governing equations

2.1. *The flow equations*

Let $\Omega_t \subset \mathbb{R}^{n_{sd}}$ and $(0, T)$ be the spatial and temporal domains respectively, where n_{sd} is the number of space dimensions, and let Γ_t denote the boundary of Ω_t. The spatial and temporal coordinates are denoted by $\boldsymbol{x}$ and t. The Navier–Stokes equations governing incompressible fluid flow are

$$\rho\left(\frac{\partial \boldsymbol{u}}{\partial t} + \boldsymbol{u}\cdot\boldsymbol{\nabla}\boldsymbol{u} - \boldsymbol{f}\right) - \boldsymbol{\nabla}\cdot\boldsymbol{\sigma} = 0 \quad \text{on } \Omega_t \text{ for } (0, T), \tag{2.1}$$

$$\boldsymbol{\nabla}\cdot\boldsymbol{u} = 0 \quad \text{on } \Omega_t \text{ for } (0, T). \tag{2.2}$$

Here ρ, $\boldsymbol{u}$, $\boldsymbol{f}$ and $\boldsymbol{\sigma}$ are the density, velocity, body force and the stress tensor, respectively. The stress tensor is written as the sum of its isotropic and deviatoric parts:

$$\boldsymbol{\sigma} = -p\boldsymbol{I} + \boldsymbol{T}, \quad \boldsymbol{T} = 2\mu\boldsymbol{\varepsilon}(\boldsymbol{u}), \quad \boldsymbol{\varepsilon}(\boldsymbol{u}) = \tfrac{1}{2}((\boldsymbol{\nabla}\boldsymbol{u}) + (\boldsymbol{\nabla}\boldsymbol{u})^T), \tag{2.3}$$

where p and μ are the pressure and dynamic viscosity, respectively. Both the Dirichlet and Neumann-type boundary conditions are accounted for, represented as

$$\boldsymbol{u} = \boldsymbol{g} \text{ on } (\Gamma_t)_g, \quad \boldsymbol{n}\cdot\boldsymbol{\sigma} = \boldsymbol{h} \text{ on } (\Gamma_t)_h, \tag{2.4}$$

where $(\Gamma_t)_g$ and $(\Gamma_t)_h$ are complementary subsets of the boundary Γ_t and $\boldsymbol{n}$ is its unit normal vector. The initial condition on the velocity is specified on Ω_t at $t = 0$:

$$\boldsymbol{u}(\boldsymbol{x}, 0) = \boldsymbol{u}_0 \quad \text{on } \Omega_0, \tag{2.5}$$

where $\boldsymbol{u}_0$ is divergence free.

2.2. *The equations of motion for a rigid body*

The rigid body motion due to the fluid forces acting on it, in the two directions along the Cartesian axes, is governed by the following equations:

$$\ddot{X} + 4\pi F_n \zeta \dot{X} + (2\pi F_n)^2 X = \frac{2C_D}{\pi M} \qquad \text{for } (0, T), \tag{2.6}$$

$$\ddot{Y} + 4\pi F_n \zeta \dot{Y} + (2\pi F_n)^2 Y = \frac{2C_L}{\pi M} \qquad \text{for } (0, T). \tag{2.7}$$

Here, ζ is the structural damping coefficient while C_L and C_D are the instantaneous lift and drag coefficients for the body, respectively. The springs in both the transverse and in-line directions are assumed to be linear and with the same stiffness. The non-dimensional mass of the body is defined as $M = 4m/(\pi\rho D^2)$ where m is the actual mass of the oscillator per unit length and ρ is the density of the fluid. The free-stream flow is assumed to be along the x-axis. $\ddot{X}$, $\dot{X}$ and X denote the normalized in-line acceleration, velocity and displacement of the body, respectively, while $\ddot{Y}$, $\dot{Y}$ and Y represent the same quantities associated with the cross-flow motion. The displacement and velocity of the cylinder are normalized by D and U_∞, respectively.

3. Finite-element formulation

To accommodate the motion of the cylinder and the deformation of the mesh, the deforming spatial domain/stabilized space-time (DSD/SST) method (Tezduyar *et al.* 1992*a*, *b*; Singh & Mittal 2005) is utilized. Equal-in-order basis functions for velocity and pressure that are bilinear in space and linear in time are used. The nonlinear equation systems resulting from the finite-element discretization of the flow equations are solved using the generalized minimal residual (*GMRES*) technique in conjunction with diagonal preconditioners. A global linear stability analysis of the combined equation system for the flow and cylinder motion is also carried out using a finite-element formulation similar to that described in Mittal & Kumar (2003). For the stability analysis, the governing equations for the flow are written in a frame of reference attached to the body. First, the steady-state solutions at various *Re*, for the stationary cylinder, are obtained by solving the governing equations without the unsteady terms. The linear stability analysis of these steady states involves the solution to an eigenvalue problem. A sub-space iteration procedure in conjunction with shift-invert transformation is utilized. The real part of the rightmost eigenvalue gives the growth rate of the most unstable mode, while the imaginary part is related to the vortex-shedding/cylinder vibration frequency.

4. The problem description

4.1. *Boundary conditions*

A no-slip condition is applied to the velocity at the cylinder boundary. The location and velocity of the cylinder are updated at each nonlinear iteration via the solution to the equations of motion for the oscillator. Free-stream values are assigned for the velocity at the upstream boundary. The viscous stress vector is set to zero at the downstream boundary. On the upper and lower boundaries, the component of velocity normal to and the component of stress vector along these boundaries are prescribed zero value.

4.2. *Finite-element mesh and the mesh moving scheme*

The finite-element mesh used for most of the computations in this paper consists of 24 604 nodes and 24 230 quadrilateral, four-noded elements. We refer to this mesh as *M24k*. The cylinder resides in a computational domain whose outer boundary is a square of edge length $100D$. The upstream, downstream and lateral boundaries are each located at $H_o = 50D$ from the centre of the cylinder.

A mesh moving scheme, in conjunction with the space–time method, is used that does not require any 'remeshing' and, consequently, is devoid of projection errors. The mesh consists of two major parts: that between the cylinder and a square box of edge

Mesh	Nodes	Elements	H_o	St	Y	X	$C_{L_{max}}$	$\overline{C}_D$
M24k	24 604	24 230	$50D$	0.1124	0.605	0.0086	0.3240	2.009
M46k	46 410	45 900	$50D$	0.1122	0.599	0.0083	0.3104	2.007
M41k	41 680	41 175	$100D$	0.1122	0.604	0.0086	0.3268	1.998

TABLE 1. $Re = 25$ flow past a freely vibrating cylinder: summary of the finite-element mesh, aerodynamic coefficients and cylinder oscillation amplitudes.

length 7D and the rest that fills in the volume between this square box and the outer boundary. The location of the outer boundary is fixed. The mesh around the cylinder, in the square box, moves along with it as a rigid body. With this arrangement, the movement of the cylinder causes deformation of only the elements lying between the square region and the outer boundary. More details on the mesh moving scheme can be found in Mittal & Kumar (1999).

5. Validation of method and convergence of results

5.1. *Flow past a stationary cylinder*

To ascertain the accuracy of the formulation and its implementation, computations are carried out for flow past a stationary cylinder for $Re = 45$, 50 and 100. Computations for $Re = 45$ result in a stable and steady flow even when the flow is perturbed. An unsteady solution is realized for $Re = 50$ and 100. For the $Re = 50$ flow, the mean drag coefficient ($\overline{C}_D$), amplitude of lift coefficient ($C_{L_{max}}$) and Strouhal number (St), for the fully developed unsteady flow, are 1.416, 0.0499 and 0.123, respectively. St is based on the time variation of the lift coefficient. The corresponding values for the $Re = 100$ flow are 1.33, 0.326 and 0.163. These values are in good agreement with those reported by other researchers. For example, Henderson (1995) reports $\overline{C}_D = 1.35$. The experimental value of St reported by Williamson (1989) is 0.1648 for parallel shedding, while Kravchenko, Moin & Shariff (1989) and Persillon & Braza (1998) report $St = 0.164$ from their simulations. The value for $C_{L_{max}}$ reported by Kravchenko *et al.* (1989) is 0.314.

5.2. *Effect of the size of the computational domain and the finite-element mesh*

The effect of mesh resolution and the location of the outer computational boundary, for a vibrating cylinder, is investigated. The $Re = 25$ case is chosen for the study, as it is associated with close to maximum amplitude of cylinder oscillations (figure 1). The details of the finite-element mesh and a summary of the results obtained are given in table 1. Meshes *M24k* and *M46k* have the same domain size. However, the spatial mesh resolution is higher in *M46k*, especially close to the cylinder. *M24k* and *M41k* have comparable spatial resolution. However, for *M41k*, the computational boundaries are located at $H_o = 100D$ from the centre of the cylinder. It is seen that all the results are in good agreement. This reflects the adequacy of mesh *M24k* in computing these flows.

6. Vortex-induced vibrations

To encourage high-amplitude oscillations, the structural damping coefficient is set to zero. The non-dimensional mass of the cylinder is $M = 4.73$. The reduced natural frequency of the spring–mass system is $F_n = 3.1875/Re$. Recall that $St \sim 0.12$ at $Re_{c0} \sim 47$. $F_n = 0.12$ is realized at $Re \sim 26.6$. Such a set-up is chosen in the hope that the aeroelastic instability might be excited for $Re < Re_{c0}$.

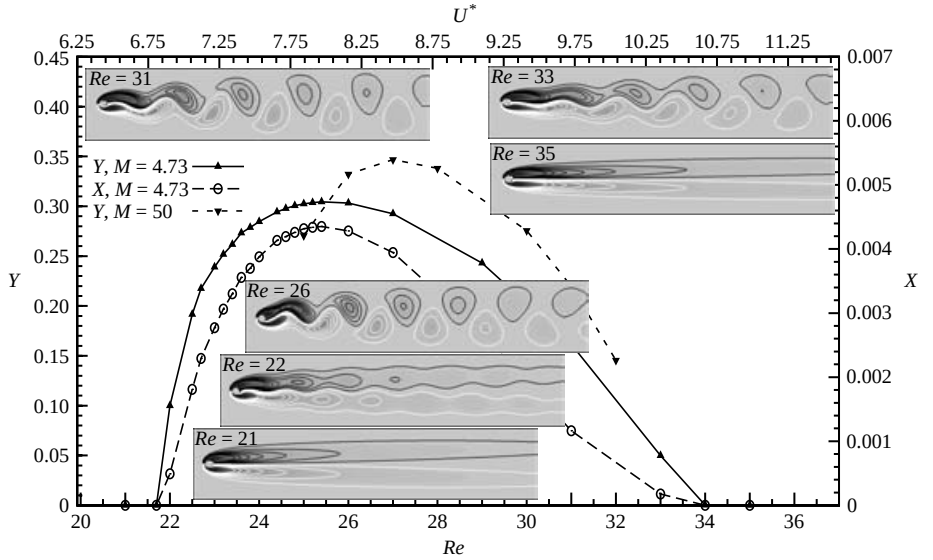

FIGURE 1. Flow past a freely vibrating cylinder with $F_n = 3.1875/Re$: amplitude of the cylinder response (normalized with its diameter) and the vorticity field at various *Re*. Contour lines in white correspond to positive vorticity while those in black denote negative vorticity.

6.1. *Overview*

Figure 1 shows the response of the cylinder at various *Re*, together with the vorticity fields at selected values of *Re*. The cylinder exhibits self-excited oscillations beyond $Re \sim 21.7$. The maximum amplitude is achieved at $Re \sim 26$ and the cylinder ceases to vibrate beyond $Re \sim 34$. As expected, the amplitude of transverse oscillations is much larger than in-line oscillations. The strength of the shed vortices correlates well with the oscillation amplitude of the cylinder. Clearly, compared to rigid supports, the elastic supports result in a significantly lower Re_c for the onset of vortex shedding. This is in line with the findings of Cossu & Morino (2000) from their global stability analysis and Buffoni (2003) from experimental observations of forced vibrations of the cylinder.

Figure 2 shows the variation with *Re* of the non-dimensional frequency of the transverse vibrations of the cylinder. Also shown are *St* and *Re* at the onset of the instability from the global linear stability analysis (LSA). The critical *Re* as well as the corresponding *St* from the LSA and direct numerical simulations (DNS) are in excellent agreement. The real and imaginary parts of the most unstable eigenmode from the LSA at the onset of the instability at both the lower and higher limits of *Re* are shown in figure 2 along with the perturbation fields from the DNS. The DNS solutions shown are those from which the steady-state solution for the stationary cylinder has been subtracted. The perturbations from the DNS appear quite similar to the eigenmodes except for the slight asymmetry about the cylinder centreline. This asymmetry is because of the nonlinear effects at $Re = 22$ and 33.5, as a result of finite-amplitude oscillations. The modes of vortex shedding for the oscillating cylinder are very similar to that observed for a stationary cylinder beyond Re_{c0} for Hopf bifurcation (Mittal & Kumar 2003), except for the difference in the shedding frequency which is reflected in the longitudinal spacing between the vortices.

6.2. *Lock-in and the effect of M*

Lock-in/synchronization (Williamson & Govardhan 2004) is observed in all the cases: the cylinder vibration frequency matches the vortex shedding frequency. It is seen

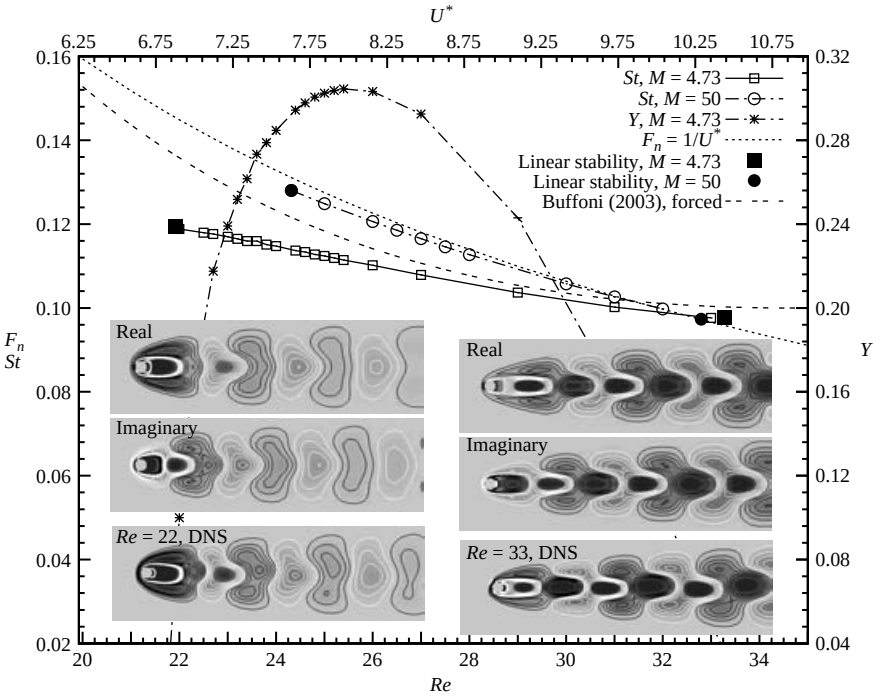

FIGURE 2. Flow past a freely vibrating cylinder with $F_n = 3.1875/Re$: non-dimensional vibration (and vortex-shedding) frequency and the amplitude of the cylinder response. Also shown are the perturbation fields from the DNS and the real and imaginary parts of the vorticity fields corresponding to the most unstable eigenmode at the onset of the instability from the LSA ($Re = 21.93$ on the left and $Re = 33.27$ on the right).

from figure 2 that for low M ($=4.73$), F_n and St are quite different. It has been observed in the past for higher Re (Williamson & Govardhan 2004; Mittal & Kumar 1999), that for low M, St for a freely vibrating cylinder does not match F_n. However, they come closer for higher M. To check whether similar behaviour is observed at subcritical Re, computations are carried out for a heavier cylinder with $M = 50$. It is found that for larger M ($= 50$), the range of Re where the self-excited oscillations are observed is smaller but St is closer to F_n. In this respect, VIV at sub- and super-critical Re show the same behaviour. Interestingly, the peak oscillation amplitude is realized at different Re for the two values of M and the peak is higher for the heavier oscillator (figure 1). This is because, for a fixed U^*, St is different for cylinders with different M. We will show later that the amplitude of C_L experienced by the cylinder depends not only on its vibration amplitude but also on the frequency of the oscillations. Consequently, the heavier cylinder experiences a lift coefficient of larger amplitude.

Also shown in figure 2 is the vortex shedding frequency, at various Re, proposed by Buffoni (2003) through observations for low-amplitude forced vibrations of the cylinder. Vortex shedding, accompanied by lock-in, was observed in his experiments for Re beyond 25. There is some difference between the results from his experiments and the present computations for free vibrations. While his curve represents, at each Re, the frequency where the vortex shedding is most intense, St in the present computations is the shedding freqency at certain values of M, Re and F_n.

Unlike at higher Re (Khalak & Williamson 1999) and for $Re \sim 100$ (Singh & Mittal 2005) no hysteresis is observed in the present case; the computations with increasing and decreasing U^* lead to the same results as shown in figure 1. The computations

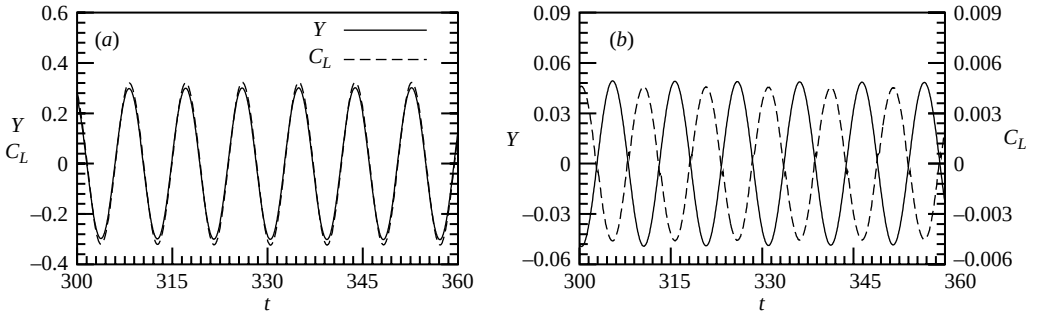

FIGURE 3. Flow past a freely vibrating cylinder with $F_n = 3.1875/Re$: time histories of the lift coefficient and the cross-flow cylinder response. (*a*) $Re = 25$, (*b*) $Re = 33$.

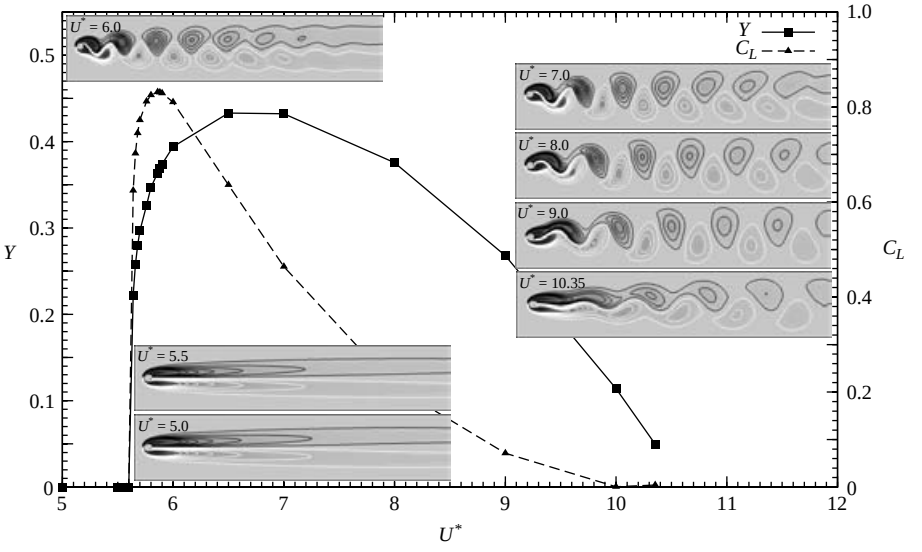

FIGURE 4. $Re = 33$ flow past a freely vibrating cylinder: amplitude of the cylinder response and the vorticity field at various U^*.

for the increasing/decreasing U^* are carried out by using the fully developed flow for a lower/higher U^* as an initial condition. The increment in U^* for the study is 0.02.

Figure 2 shows that $St \sim F_n$ at $Re = 33$. Despite the forcing and natural frequencies being same, a low-amplitude response is observed at $Re = 33$. In comparison, a higher amplitude response is seen at lower Re even when St and F_n are quite different. The time histories of the aerodynamic forces and the cylinder motion for $Re = 25$ and 33 are shown in figure 3. It is found that at $Re = 33$ the lift coefficient and transverse oscillations of the cylinder are out of phase. They are in phase for $Re = 25$, where the cylinder exhibits high-amplitude oscillations. The flow at $Re = 33$ for various U^* is studied in further detail in § 6.3.

6.3. $Re = 33$, *variation with* U^*

A computational experiment is conducted to study the behaviour of the oscillator for various values of U^* while Re for the flow, based on the free-stream speed, is held constant. The amplitude of the cylinder oscillations and lift coefficient at various U^* is shown in figure 4. The aeroelastic instability is excited for $U^* > 5.6$, reaches a maximum at $U^* \sim 6.5$ and ceases beyond $U^* \sim 10.4$. St, along with the amplitude of

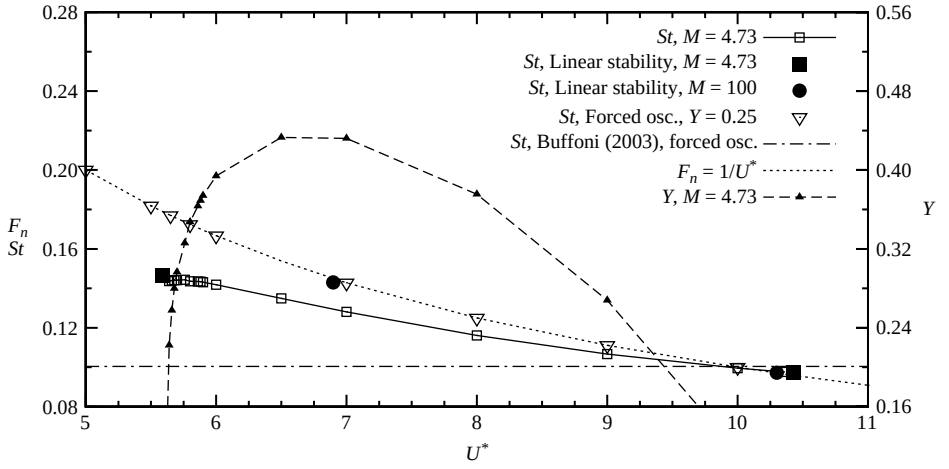

FIGURE 5. $Re = 33$ flow past a freely vibrating cylinder: the the non-dimensional vibration frequency and amplitude of the cylinder response. Also shown is F_n and the shedding frequency reported by Buffoni (2003).

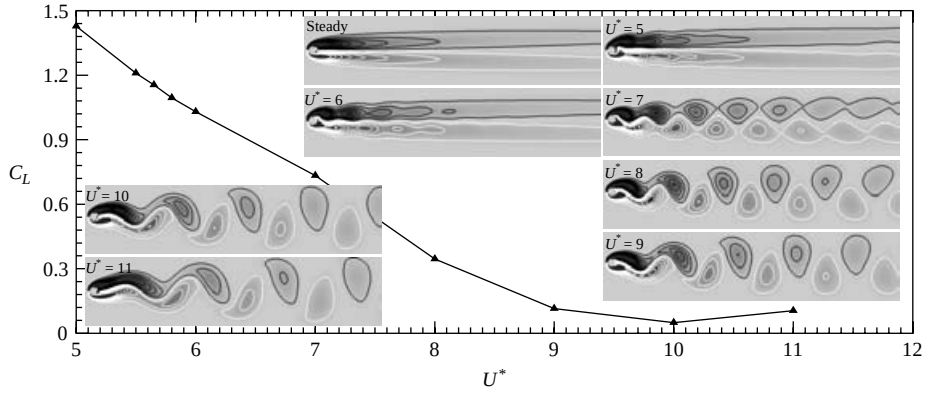

FIGURE 6. $Re = 33$ flow past a cylinder with forced vibrations of amplitude $0.25D$: amplitude of the lift coefficient and the vorticity field at various U^*.

cylinder vibration, is shown in figure 5. As was seen earlier, the cylinder vibration frequency approaches the natural frequency for larger values of M. There is good agreement on the onset of the instability from the DNS and LSA. These results explain the observation in § 6.2 regarding the low amplitude of oscillations for $Re = 33$. Results for $Re \sim 100$ can be seen in Singh & Mittal (2005). It is expected that the range of U^* for which the system exhibits self-excited oscillations and the value of U^* at which peak vibration amplitude is realized varies with Re.

6.4. *Forced vibrations,* $Re = 33$, $Y = 0.25D$

It can be noticed on figure 4 that the maximum amplitudes of the lift coefficient and cylinder vibrations occur at different U^*. To address this issue, we seek an answer to a related question: does forced vibration at different frequencies but the same oscillation amplitude result in the same amplitude of the lift coefficient? Results for the computations with forced vibrations of the cylinder at fixed amplitude ($= 0.25D$) and various frequencies are shown in figures 5 and 6. St for the most intense vortex shedding from the forced vibration experiments from Buffoni (2003) for low-amplitude vibrations is also shown in figure 5. In all the cases vortex shedding is observed and

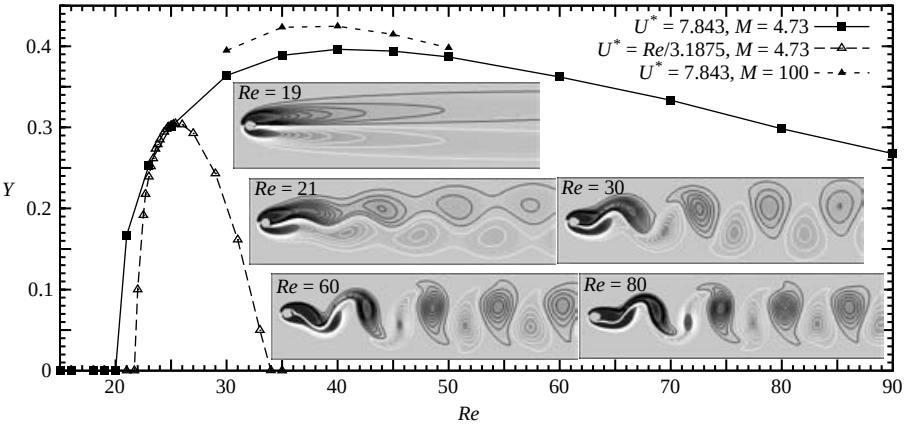

FIGURE 7. $U^* = 7.843$ flow past a freely vibrating cylinder: amplitude of the cylinder response and the vorticity field at various Re. Also shown is the response of the cylinder for $F_n = 3.1875/Re$.

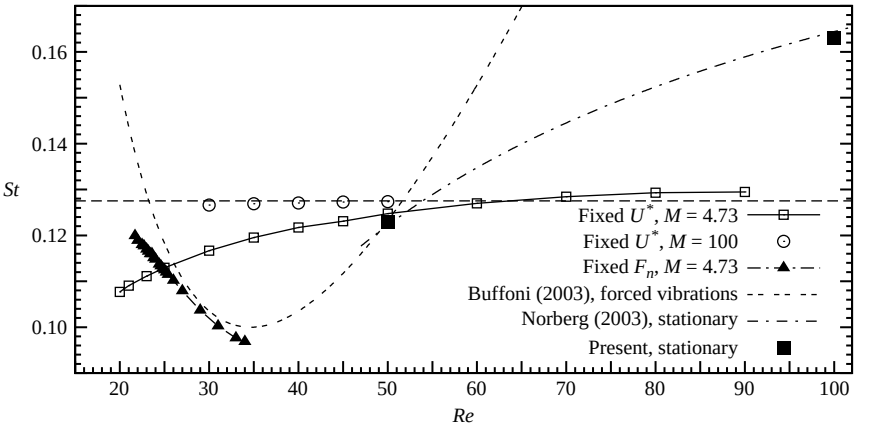

FIGURE 8. $U^* = 7.843$ flow past a freely vibrating cylinder: the non-dimensional vibration frequency and the amplitude of the cylinder response. Also shown is the normalized natural frequency of the oscillator and results from other researchers.

its frequency matches the oscillation frequency. As seen from figure 6, there is a significant variation in the amplitude of the lift coefficient with U^* including a non-monotonic behaviour for a certain range of U^*. This shows that the amplitude of the lift coefficient depends not only on the amplitude of cylinder vibrations, but also on the frequency of oscillations. Alternatively, to generate the same C_L amplitude for different U^*, one would require a different amplitude of cylinder vibrations.

6.5. $U^* = 7.843$ ($F_n = 0.1275$), *variation with Re*

Figure 1 shows that the maximum amplitude of cylinder vibrations, when F_n is held fixed (F_n varies as $1/Re$), is achieved for $F_n = 0.126$. To investigate the effect of Re, computations are carried out for a fixed value of U^*. Figures 7 and 8 show the results of this study. Vortex shedding and cylinder vibrations are observed for Re as low as ~ 20. It is possible that Re_c for an elastically mounted cylinder is even lower than this value. To identify the exact value, a similar analysis should be carried out for various values of U^* and M. Other than the frequency of vortex shedding, the unsteady flows at sub- and super-critical Re (for example, at $Re = 30$ and 60) appear quite similar.

Unlike the previous cases, vortex shedding takes place for all $Re > Re_c$. The maximum amplitude of transverse vibrations ($\sim 0.4D$, for $M = 4.73$) is observed at $Re \sim 40$. The vortex-shedding (and cylinder vibration) frequency is shown in figure 8. The trends in the variation of St with Re are quite different for the cases with varying versus fixed F_n. Also plotted in figure 8 are the variations in St for a stationary cylinder and for forced vibrations. As was observed earlier, the heavier oscillator results in St close to F_n.

7. Conclusions

A stabilized finite-element method has been used to study vortex shedding at sub-critical Re. Self-excited oscillations, accompanied by vortex shedding, are possible at Re as low as 20. The results are confirmed via a global linear stability analysis. Transverse oscillations of amplitude up to $\sim 0.45D$ have been observed for sub-critical Re. Lock-in is observed in all cases. However, the mass of the oscillator plays a major role in determining the range of U^* for which the oscillator is self-excited and the proximity of F_n and St. For the same reason, a heavier oscillator may exhibit oscillations of higher amplitude. Unlike for $Re > Re_{c0}$, no hysteresis is observed for sub-critical Re.

Partial support for this work from the Department of Science & Technology, India is gratefully acknowledged.

REFERENCES

Buffoni, E. 2003 Vortex shedding in subcritical conditions. *Phys. Fluids* **15**, 814–816.

Cossu, C. & Morino, L. 2000 On the instability of a spring-mounted circular cylinder in a viscous flow at low Reynolds numbers. *J. Fluids Struct.* **14**, 183–196.

Henderson, R. D. 1995 Details of the drag curve near the onset of vortex shedding. *Phys. Fluids* **7**, 2102–2104.

Khalak, A. & Williamson, C. H. K. 1999 Motions, forces and mode transitions in vortex-induced vibrations at low mass-damping. *J. Fluids Struct.* **13**, 813–851.

Kravchenko, A. G., Moin, P. & Shariff, K. 1999 B-Spline method and zonal grids for simulations of complex turbulent flows. *J. Comput. Phys.* **151**, 757–789.

Mittal, S. & Kumar, V. 1999 Finite element study of vortex-induced cross-flow and in-line oscillations of a circular cylinder at low Reynolds numbers. *Intl J. Numer. Meth. Fluids* **31**, 1087–1120.

Mittal, S. & Kumar, B. 2003 Flow past a rotating cylinder. *J. Fluid Mech.* **476**, 303–334.

Mittal, S. & Tezduyar, T. E. 1992 A finite element study of incompressible flows past oscillating cylinders and airfoils. *Intl J. Numer. Meth. Fluids* **15**, 1073–1118.

Norberg, C. 2003 Fluctuating lift on a circular cylinder: review and new measurements. *J. Fluids Struct.* **17**, 57–96.

Persillon, H. & Braza, M. 1998 Physical analysis of the transition to turbulence in the wake of a circular cylinder by three-dimensional Navier-Stokes simulation. *J. Fluid Mech.* **365**, 23–88.

Singh, S. P. & Mittal, S. 2005 Vortex induced oscillations at low Reynolds numbers: hysteresis & vortex-shedding modes. *J. Fluids Struct.* (to appear).

Tezduyar, T. E., Behr, M. & Liou, J. 1992*a* A new strategy for finite element computations involving moving boundaries and interfaces – the deforming-spatial-domain/space-time procedure: I. The concept and the preliminary tests. *Comput. Meth. Appl. Mech. Engng* **94**(3), 339–351.

Tezduyar, T. E., Behr, M., Mittal, S. & Liou J. 1992*b* A new strategy for finite element computations involving moving boundaries and interfaces – the deforming-spatial-domain/space-time procedure: II. Computation of free-surface flows, two-liquid flows, and flows with drifting cylinders. *Comput. Meth. Appl. Mech. Engng* **94**(3), 353–371.

Williamson, C. H. K. 1989 Oblique and parallel modes of vortex shedding in the wake of a circular cylinder at low Reynolds numbers. *J. Fluid Mech.* **206**, 579–627.

Williamson, C. H. K. & Govardhan, R. 2004 Vortex-induced vibration. *Ann. Rev. Fluid Mech.* **36**, 413–455.